HIGH-ORDER WENO-Θ6 FINITE VOLUME METHOD FOR TWO-DIMENSIONAL COMPRESSIBLE EULER EQUATIONS

Nguyen Minh Hieu Pham, Thien Binh Nguyen*
Vietnamese-German University, Vietnam

*Corresponding author: binh.nt@vgu.edu.vn

(Received: March 02, 2026; Revised: May 21, 2026; Accepted: June 16, 2026)
DOI: 10.31130/ud-jst.2026.24(6A).112E

Abstract - A high-order finite-volume WENO-θ6 method is proposed for two-dimensional compressible Euler equations. The method employs θ-adaptive weighting to combine fifth-order upwind and sixth-order central reconstructions based on local smoothness indicators, performed in characteristic fields to enhance stability near sharp gradients and discontinuities. The conservation property is naturally preserved within the finite-volume framework. We validate the proposed scheme against WENO-Z5 and WENO-Z6 on standard benchmark problems in computational fluid dynamics, including shock tube problems, Rayleigh–Taylor and Kelvin–Helmholtz instabilities, Double Mach Reflection, Forward-Facing Step, and 2D Riemann problems. Results demonstrate that WENO-θ6 achieves sixth-order accuracy in smooth regions, captures shocks sharply without spurious oscillations, resolves fine vortical structures with lower numerical dissipation, and maintains solution symmetry, proving the method a reliable, strictly conservative tool for compressible flow simulations.

Key words - High-order finite-volume WENO-θ6 scheme; two-dimensional compressible Euler equations; Finite Volume Method; Shock Capturing; Riemann problems; Computational Fluid Dynamics

1. Introduction

Wave propagation, as a result of convective processes, is central to numerical simulations in computational fluid dynamics [1], [2], [3], meteorology, astrophysics [4], and electromagnetism [5], [6]. The governing hyperbolic PDEs, such as the compressible Euler, MHD, and Maxwell equations, support both smooth waves and strong discontinuities (e.g., shocks and contacts), making accurate numerical approximation a challenging task.

A feasible numerical scheme for hyperbolic PDEs must be capable of suppressing non-physical spurious oscillations in the vicinity of strong gradients or discontinuities while retaining high-order accuracy in smooth regions. Early Total Variation Diminishing (TVD) methods [7], [8] resolve oscillations, yet the accuracy is degraded near extrema. To address this drawback, Harten *et. al.* introduced Essentially Non-Oscillatory (ENO) schemes [9] - [12], followed by the Weighted ENO (WENO) schemes of Liu et al. [13]. WENO methods use a nonlinear convex combination of reconstruction stencils, adaptively weighting them to achieve high-order accuracy in smooth regions and non-oscillatory behavior at discontinuities.

Key advances in WENO methods include the classical fifth-order WENO-JS scheme by Jiang and Shu [14] - [17], and subsequent works aim at reducing dissipation near critical points, such as Mapped WENO (WENO-M) [18] and WENO-Z [19, 20]. To further improve accuracy and spectral properties, a number of sixth-order schemes have been proposed, including WENO-NW6 [21], [22], WENO-CU6 [23], WENO-Z6 [24], WENO6-S [25], and WENO-CZ6 [26].

The WENO-θ6 scheme, originally developed by Jung and Nguyen [27] in a finite-difference (FD) framework, introduces an adaptive combination mechanics between an upwind five-point and a central six-point reconstruction stencil. By employing a new set of symmetric smoothness indicators and a tunable parameter θ, it excels at identifying optimal stencils. However, most existing WENO-θ6 implementations are limited to one-dimensional or dimension-by-dimension (DbD) FD approaches. In contrast, FVM generally offers greater flexibility for complex geometries and naturally preserves conservation for calculating quantities. Extending WENO-θ6 to a fully two-dimensional FVM framework, therefore, requires careful formulation.

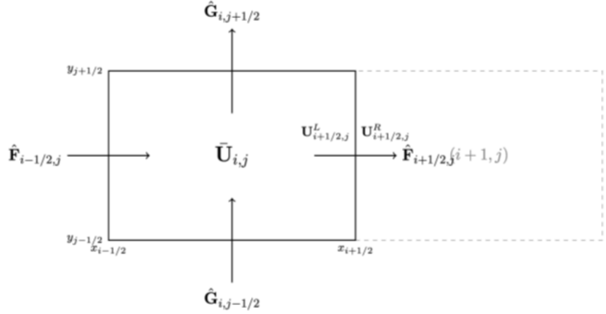

Figure 1. *FV discretization of a 2D Cartesian control volume using cell-averaged conserved variables and WENO-θ6 reconstruction at cell interfaces*

This paper adapts the sixth-order WENO-θ6 method to a two-dimensional finite-volume framework, which is more common in finite difference schemes. We create a consistent FVM approach using dimension-by-dimension (DbD) reconstruction to improve efficiency and maintain strict conservation. By introducing symmetric smoothness indicators and an adaptive weighting system, we show that the scheme can resolve small-scale vortical structures, Kelvin-Helmholtz (KH) instabilities, sharp shocks, and complex wave interactions in different flow configurations. We validate the method accuracy, efficiency, robustness, and stability via a selective number of two-dimensional benchmark problems in computational fluid dynamics. These include shock tube problems, the Rayleigh – Taylor instability, the implosion problem, the

Double Mach Reflection at Mach 10, the Mach 3 Forward-Facing Step, and 2D Riemann problems involving shocks, rarefactions, and contact discontinuities. These tests show that the WENO-θ6 FVM is a high-fidelity tool for detailed flow physics, offering lower computational cost than full multidimensional reconstruction.

2. Governing Equations and Discretization Framework

The governing equations for the two-dimensional flow of an inviscid, compressible fluid are the Euler equations. This system is written in conservative form; in Cartesian coordinates, the differential form reads:

$$\frac{\partial \mathbf{U}}{\partial t}+\frac{\partial \mathbf{F}(\mathbf{U})}{\partial x}+\frac{\partial \mathbf{G}(\mathbf{U})}{\partial y}=0, \tag{1}$$

where $\mathbf{U}$ is the vector of conserved state variables, and $\mathbf{F}(\mathbf{U})$ and $\mathbf{G}(\mathbf{U})$ are the convective flux vectors in the x- and y-directions, respectively. These are defined as:

$$\mathbf{U}=\begin{pmatrix}\rho\\ \rho u\\ \rho v\\ E\end{pmatrix}, \mathbf{F}(\mathbf{U})=\begin{pmatrix}\rho u\\ \rho u^2+p\\ \rho u v\\ (E+p)u\end{pmatrix}, \mathbf{G}(\mathbf{U})=\begin{pmatrix}\rho v\\ \rho u v\\ \rho v^2+p\\ (E+p)v\end{pmatrix}. \tag{2}$$

Here, ρ is the fluid density, (u, v) are the velocity components, and p is the pressure. The total energy per unit volume, E, is the sum of the internal energy and the kinetic energy:

$$E=\rho e+\frac{1}{2}\rho(u^2+v^2), \tag{3}$$

where e is the specific internal energy. To close this system, the equation of state for an ideal gas is to constitute the relation between pressure and the total energy, which is given as follows:

$$p=(\gamma-1)\left(E-\frac{1}{2}\rho(u^2+v^2)\right)=(\gamma-1)\rho e, \tag{4}$$

where γ is the ratio of specific heats. In this work, we choose $\gamma=1.4$ throughout this study.

We discretize the computational domain into non-overlapping rectangular cells $I_{i,j}$, defined as:

$$I_{i,j}=\left[x_{i-\frac{1}{2}}, x_{i+\frac{1}{2}}\right]\times\left[y_{j-\frac{1}{2}}, y_{j+\frac{1}{2}}\right], \tag{5}$$

with uniform grid spacings Δx and Δy. The FV method evolves the cell-averaged conservative variables, defined as:

$$\bar{\mathbf{U}}_{i,j}(t)=\frac{1}{\Delta x\Delta y}\int_{x_{i-\frac{1}{2}}}^{x_{i+\frac{1}{2}}}\int_{y_{j-\frac{1}{2}}}^{y_{j+\frac{1}{2}}}\mathbf{U}\,(x,y,t)\,dxdy. \tag{6}$$

By integrating the governing equations over the control volume $I_{i,j}$ and applying the divergence theorem, we obtain the semi-discrete form:

$$\frac{d\bar{\mathbf{U}}_{i,j}}{dt}=-\frac{1}{\Delta x}\left(\widehat{\mathbf{F}}_{i+\frac{1}{2},j}-\widehat{\mathbf{F}}_{i-\frac{1}{2},j}\right)-\frac{1}{\Delta y}\left(\widehat{\mathbf{G}}_{i,j+\frac{1}{2}}-\widehat{\mathbf{G}}_{i,j-\frac{1}{2}}\right), \tag{7}$$

where $\widehat{\mathbf{F}}_{i\pm1/2,j}$ and $\widehat{\mathbf{G}}_{i,j\pm1/2}$ represent the numerical fluxes across the cell interfaces. In this work, the left and right interface states are obtained using a DbD WENO-θ6 reconstruction applied to the cell-averaged conservative variables.

High-order accuracy is achieved by replacing the physical fluxes in Eq. (2) with numerical fluxes that depend on the reconstructed values of the conservative variables at the cell interfaces. Specifically, we require high-order approximations of $\mathbf{U}_{\mathrm{i}+\frac{1}{2},\mathrm{j}}$ at the interface locations from the left (L) and right (R) sides. This reconstruction step, described in detail in Sec. 3, is critical for determining the spatial accuracy and stability of the scheme.

3. The High-Order WENO-θ6 Reconstruction

3.1. The Adaptive WENO-θ6 Reconstruction

In this section, we describe finite-volume WENO-θ6 solution reconstruction technique [28]. The method is based on a novel adaptive weighting strategy that linearly combines fifth- and sixth-order approximations to achieve optimal resolution properties.

3.1.1. Adaptive Linear Reconstruction

The core idea of the WENO-θ6 scheme is to combine the fifth-order upwind reconstruction (using sub-stencils $\mathrm{S}_0, \mathrm{S}_1, \mathrm{S}_2$) and the sixth-order central reconstruction (adding S_3) in a unified framework. Optimally, the high-order reconstructed value $\mathbf{U}_{\mathrm{i}+1/2}^{L}$ on the left side of a cell interface $\mathrm{x}_{\mathrm{i}+1/2}$ is approximated as a linear combination of the third-order reconstructed values $\mathbf{U}_{\mathrm{i}+\frac{1}{2}}^{\mathrm{L,k}}$ over each sub-stencil S_k, $\mathrm{k}=0,1,2,3$:

$$\mathbf{U}_{\mathrm{i}+\frac{1}{2}}^{\mathrm{L}}=\sum_{k=0}^{3}\gamma_k^\theta\,\mathbf{U}_{\mathrm{i}+\frac{1}{2}}^{\mathrm{L,k}}, \tag{8a}$$

$$\mathbf{U}_{\mathrm{i}+\frac{1}{2}}^{\mathrm{L,0}}=\frac{2}{6}\bar{\mathbf{U}}_{\mathrm{i}-2}-\frac{7}{6}\bar{\mathbf{U}}_{\mathrm{i}-1}+\frac{11}{6}\bar{\mathbf{U}}_{\mathrm{i}}, \tag{8b}$$

$$\mathbf{U}_{\mathrm{i}+\frac{1}{2}}^{\mathrm{L,1}}=-\frac{1}{6}\bar{\mathbf{U}}_{\mathrm{i}-1}+\frac{5}{6}\bar{\mathbf{U}}_{\mathrm{i}}+\frac{2}{6}\bar{\mathbf{U}}_{\mathrm{i}+1}, \tag{8c}$$

$$\mathbf{U}_{\mathrm{i}+\frac{1}{2}}^{\mathrm{L,2}}=\frac{2}{6}\bar{\mathbf{U}}_{\mathrm{i}}+\frac{5}{6}\bar{\mathbf{U}}_{\mathrm{i}+1}-\frac{1}{6}\bar{\mathbf{U}}_{\mathrm{i}+2}, \tag{8d}$$

$$\mathbf{U}_{\mathrm{i}+\frac{1}{2}}^{\mathrm{L,3}}=\frac{11}{6}\bar{\mathbf{U}}_{\mathrm{i}+1}-\frac{7}{6}\bar{\mathbf{U}}_{\mathrm{i}+2}+\frac{2}{6}\bar{\mathbf{U}}_{\mathrm{i}+3}, \tag{8e}$$

The linear weights γ_k^θ are defined adaptively based on a parameter $\theta\in[0,1]$:

$$\gamma_0^\theta=\frac{1}{20}(1+\theta), \gamma_1^\theta=\frac{3}{20}(3+\theta),$$

$$\gamma_2^\theta=\frac{3}{20}(3-\theta), \gamma_3^\theta=\frac{1}{20}(1-\theta). \tag{9}$$

Here, $\theta=1$ recovers the fifth-order reconstructed $\mathbf{U}_{\mathrm{i}+1/2}^{\mathrm{L}}$ via an upwind scheme (where $\gamma_3^\theta=0$), and $\theta=0$ recovers the sixth-order reconstructed $\mathbf{U}_{\mathrm{i}+1/2}^{\mathrm{L}}$ via a central scheme.

The reconstruction of the right value $\mathbf{U}_{\mathrm{i}+1/2}^{\mathrm{R}}$ follows a similar procedure with mirrored sub-stencils S_k, k = 0, 1, 2, 3 over the interface $\mathrm{x}_{\mathrm{i}+1/2}$.

3.1.2. Nonlinear Reconstruction for Shock Capturing

The optimal linear combination given in Eq. (8) generates spurious oscillations in the vicinity of discontinuities, e.g., shocks or contacts. To handle discontinuities, we replace the linear weights γ_k^θ with nonlinear weights ω_k^θ:

$$\omega_k^\theta=\frac{\alpha_k^\theta}{\sum_{l=0}^{3}\alpha_l^\theta}, \alpha_k^\theta=\gamma_k^\theta\left(1+\left(\frac{\tau_\theta}{\beta_k+\epsilon}\right)^{\mathrm{p}}\right). \tag{10}$$

Here, β_k are the so-called smoothness indicators, which measure how smooth the solution is over each sub-stencil.

τ_θ measures the solution smoothness over the large reconstruction stencil $\mathrm{S} = \bigcup_{\mathrm{k}=0}^{3} \mathrm{S_k}$. $\epsilon = 10^{-10}$ is chosen to prevent division by zero. For a smooth problem, the nonlinear weights ω_k^θ converge to its optimal linear versions γ_k^θ to recover the sixth-order accuracy order. On the contrary, in the case of shock presence, ω_k^θ is close to zero to effectively eliminate any sub-stencil(s) containing shocks or contacts to prevent spurious oscillations to form and develop in the numerical approximation.

The smoothness indicators β_k for the sub stencils are defined as:

$$
\begin{aligned}
\beta_0 &= \tfrac{13}{12}(\bar{\mathbf{U}}_{i-2} - 2\bar{\mathbf{U}}_{i-1} + \bar{\mathbf{U}}_i)^2 + (\bar{\mathbf{U}}_{i-2} - 3\bar{\mathbf{U}}_{i-1} + 2\bar{\mathbf{U}}_i)^2, \\
&\quad , \\
\beta_1 &= \tfrac{13}{12}(\bar{\mathbf{U}}_{i-1} - 2\bar{\mathbf{U}}_i + \bar{\mathbf{U}}_{i+1})^2 + (\bar{\mathbf{U}}_i - \bar{\mathbf{U}}_{i+1})^2, \\
\beta_2 &= \tfrac{13}{12}(\bar{\mathbf{U}}_i - 2\bar{\mathbf{U}}_{i+1} + \bar{\mathbf{U}}_{i+2})^2 + (\bar{\mathbf{U}}_i - \bar{\mathbf{U}}_{i+1})^2, \\
\beta_3 &= \tfrac{13}{48}(3\bar{\mathbf{U}}_i - 7\bar{\mathbf{U}}_{i+1} + 5\bar{\mathbf{U}}_{i+2} - \bar{\mathbf{U}}_{i+3})^2 \\
&\quad + (2\bar{\mathbf{U}}_{i+1} - 3\bar{\mathbf{U}}_{i+2} + \bar{\mathbf{U}}_{i+3})^2.
\end{aligned} \tag{11}
$$

3.1.3. Adaptive Global Smoothness Indicator

The global smoothness indicator τ_θ is selected adaptively between an upwind fifth-order indicator τ_5 (based on stencil $\mathrm{S_5} = \bigcup_{\mathrm{k}=0}^{2} \mathrm{S_k}$) and a central sixth-order indicator τ_6 (based on stencil $\mathrm{S_6} = \bigcup_{\mathrm{k}=0}^{3} \mathrm{S_k}$) to balance accuracy and stability.

The fifth-order smoothness indicator τ_5 is defined as:

$$
\begin{aligned}
\tau_5 &= \tfrac{13}{12}(\bar{\mathbf{U}}_{i-2} - 4\bar{\mathbf{U}}_{i-1} + 6\bar{\mathbf{U}}_i - 4\bar{\mathbf{U}}_{i+1} + \bar{\mathbf{U}}_{i+2})^2 \\
&\quad + (-\bar{\mathbf{U}}_{i-1} + 3\bar{\mathbf{U}}_i - 3\bar{\mathbf{U}}_{i+1} + \bar{\mathbf{U}}_{i+2})^2.
\end{aligned} \tag{12}
$$

The sixth-order smoothness indicator τ_6 is defined as:

$$
\begin{aligned}
\tau_6 &= \tfrac{13}{12}(-\bar{\mathbf{U}}_{i-2} + 5\bar{\mathbf{U}}_{i-1} - 10\bar{\mathbf{U}}_i + 10\bar{\mathbf{U}}_{i+1} - 5\bar{\mathbf{U}}_{i+2} + \bar{\mathbf{U}}_{i+3})^2 \\
&\quad + \tfrac{1}{4}(\bar{\mathbf{U}}_{i-2} - 3\bar{\mathbf{U}}_{i-1} + 2\bar{\mathbf{U}}_i + 2\bar{\mathbf{U}}_{i+1} - 3\bar{\mathbf{U}}_{i+2} + \bar{\mathbf{U}}_{i+3})^2.
\end{aligned} \tag{13}
$$

To ensure robustness in regions with vanishing high-order derivatives, we augment these definitions with a regularization term C_τ:

$$
\begin{aligned}
\tau_5 &= \tau_5 + C_\tau \Delta x^6, \\
\tau_6 &= \tau_6 + C_\tau \Delta x^8.
\end{aligned} \tag{14}
$$

In our implementation, we use $C_\tau = 40$. This parameter helps the switching mechanism prioritize the sixth-order scheme in smooth regions where derivatives are close to zero.

The indicator τ_θ and the parameter θ are determined by the following switching mechanism:

$$
(\tau_\theta, \theta) = \begin{cases} (\tau_6, 0) & \text{if } \tau_6 < \tau_5, \\ (\tau_5, 1) & \text{if } \tau_6 \geq \tau_5. \end{cases} \tag{15}
$$

This mechanism ensures that in smooth regions (where $\tau_6 \ll \tau_5$), the scheme selects the full sixth-order stencil ($\theta = 0$). Near discontinuities, it reverts to the more stable fifth-order configuration ($\theta = 1$).

Finally, to enhance numerical dispersion, we deploy in this work the technique developed by Taylor et al. [29], which is given as follows.

$$
\beta_\mathrm{k} = \begin{cases} 0, \text{if } \mathrm{R}(\beta) \leq \alpha_R, \\ \beta_\mathrm{k}, \text{otherwise,} \end{cases} where\ R(\beta) = \frac{max_j(\beta_j)}{\varepsilon + min_j(\beta_j)}. \tag{16}
$$

Here, the relative threshold α_R can be tuned depending on the flow configuration, which is commonly taken to be a small number for flows with shocks or contact discontinuities. In our simulations reported in this work, except for specific configurations, we set $\alpha_R = 20$.

3.2. Multidimensional FV Implementation

This section details the construction of the two-dimensional FVM utilizing the WENO-θ6 reconstruction strategy. Roadmap: (i) we outline the cell geometry and semi-discrete update, (ii) we describe the DbD reconstruction, (iii) we project to characteristic fields and give a step-wise reconstruction recipe, and (iv) we close with the flux evaluation and its link to the FV layout in Figure 1. All spatial reconstructions are performed using a characteristic-wise WENO-θ6 procedure within a DbD FV framework.

3.2.1. DbD Reconstruction

We consider the two-dimensional system of conservation laws on a rectangular domain, discretized into cells $I_{i,j} = [x_{i-1/2}, x_{i+1/2}] \times [y_{j-1/2}, y_{j+1/2}]$ as illustrated in Figure 1. The semi-discrete conservative update for the cell average $\bar{\mathbf{U}}_{i,j}$ reads:

$$
\frac{d\bar{\mathbf{U}}_{i,j}}{dt} = -\frac{1}{\Delta x}\left(\hat{\mathbf{F}}_{i+\frac{1}{2},j} - \hat{\mathbf{F}}_{i-\frac{1}{2},j}\right) - \frac{1}{\Delta y}\left(\hat{\mathbf{G}}_{i,j+1/2} - \hat{\mathbf{G}}_{i,j-1/2}\right). \tag{17}
$$

The DbD strategy decouples the reconstruction into independent one-dimensional sweeps. For fluxes in the x-direction, we reconstruct left/right interface states $\mathbf{U}_{i+1/2,j}^L$ and $\mathbf{U}_{i+1/2,j}^R$ from the stencil along the i-index. The same implementation principle is applied to the fluxes in the y-direction. Unlike component-wise approaches, which often yield spurious oscillations, we perform this reconstruction in the local characteristic fields.

3.2.2. Characteristic Projection

For the Euler equations, the Jacobian matrices $\mathbf{A}_x = \partial\mathbf{F}/\partial\mathbf{U}$ and $\mathbf{A}_y = \partial\mathbf{G}/\partial\mathbf{U}$ are diagonalizable. At each interface $x_{i+1/2}$, we utilize the Roe average state $\hat{\mathbf{U}}$ to define the projection matrices $\mathbf{L}(\hat{\mathbf{U}})$ (left eigenvectors) and $\mathbf{R}(\hat{\mathbf{U}})$ (right eigenvectors).

The projection $\mathbf{W} = \mathbf{L}\delta\mathbf{U}$ transforms the conservative variations into characteristic variations. Explicitly, for the x-direction with eigenvalues $u - c, u, u + c$, the characteristic variables $\mathbf{W} = [w_1, w_2, w_3, w_4]^T$ (where w_2, w_3 correspond to shear and entropy waves) are related to the primitive variations by:

$$
\delta\mathbf{W} = \mathbf{L}\delta\mathbf{U} \Rightarrow \begin{cases} \delta w_1 = \frac{1}{2c^2}(\delta p - \rho c \delta u), \\ \delta w_2 = \delta\rho - \frac{1}{c^2}\delta p, \\ \delta w_3 = \delta v, \\ \delta w_4 = \frac{1}{2c^2}(\delta p + \rho c \delta u). \end{cases} \tag{18}
$$

The complete reconstruction procedure for the interface $x_{i+1/2,j}$ is:

1. **Projection:** Compute the local characteristic variables $\mathbf{v}_k = \mathbf{L}_{i+1/2}\bar{\mathbf{U}}_{k,j}$ for all stencil cells k.

2. **WENO-θ6 Step:** Apply the scalar WENO-θ6

procedure (Eqs. (8) – (16)) to each component of $\mathbf{v}_k$ to obtain $\mathbf{v}^L_{i+1/2}$ and $\mathbf{v}^R_{i+1/2}$.

3. **Recovery:** Project back to physical space: $\mathbf{U}^{L,R}_{i+1/2,j} = \mathbf{R}_{i+1/2}\mathbf{v}^{L,R}_{i+1/2}$.

This process is repeated analogously for the y-direction interfaces.

3.2.3. Numerical Flux Evaluation

In this work, we employ the Global Lax-Friedrichs (GLF) flux for its robustness in high-speed flows. The numerical flux $\hat{\mathbf{F}}_{i+1/2,j}$ is given by:

$$\hat{\mathbf{F}}_{i+\frac{1}{2},j} = \frac{1}{2}\left[\mathbf{F}\left(\mathbf{U}^L_{i+\frac{1}{2},j}\right) + \mathbf{F}\left(\mathbf{U}^R_{i+\frac{1}{2},j}\right) - \alpha_x\left(\mathbf{U}^R_{i+\frac{1}{2},j} - \mathbf{U}^L_{i+\frac{1}{2},j}\right)\right] \tag{19}$$

where $\alpha_x = \max_{i,j}(|u_{i,j}| + c_{i,j})$ is the global maximum wave speed.

3.3. Temporal Discretization and Stability

The semi-discrete scheme described in Sec. 2 results in a system of Ordinary Differential Equations (ODEs) for each cell (i, j):

$$\frac{d\bar{\mathbf{U}}_{i,j}}{dt} = L(\bar{\mathbf{U}}_{i,j}), \tag{20}$$

where $L(\bar{\mathbf{U}})$ is the spatial discretization operator defined by the divergence of the numerical fluxes, resulting from the finite-volume WENO-θ6 spatial discretization.

Remark 1: We note that a monotone global Lax-Friedrichs numerical flux, when coupling to a strongly stability preserving time-stepping method, as the third-order SSP-RK3 method deployed in our work in Eq. (21) below, sustains the numerical stability for smooth problems. Numerical stability of problems with discontinuities is tackled via the adaptive nonlinear WENO reconstruction procedure. Other types of numerical fluxes, e.g., HLLC, AUSM family, are under investigation and will be addressed in our subsequent works.

3.3.1. SSP-RK3 Time Integration

To integrate this system in time, we use the third-order Strong Stability Preserving Runge-Kutta (SSP-RK3) method [30]. This choice is consistent with the high spatial accuracy of the WENO scheme and ensures that the time evolution does not introduce spurious oscillations. The three stages of the SSP-RK3 scheme are:

$$\begin{aligned} \mathbf{U}^{(1)} &= \bar{\mathbf{U}}^n + \Delta t L(\bar{\mathbf{U}}^n), \\ \mathbf{U}^{(2)} &= \tfrac{3}{4}\bar{\mathbf{U}}^n + \tfrac{1}{4}\mathbf{U}^{(1)} + \tfrac{1}{4}\Delta t L(\mathbf{U}^{(1)}), \\ \bar{\mathbf{U}}^{n+1} &= \tfrac{1}{3}\bar{\mathbf{U}}^n + \tfrac{2}{3}\mathbf{U}^{(2)} + \tfrac{2}{3}\Delta t L(\mathbf{U}^{(2)}). \end{aligned} \tag{21}$$

3.3.2. CFL Condition

The time step Δt is constrained by the Courant-Friedrichs-Lewy (CFL) condition for stability. For a 2D Cartesian grid, it is calculated as:

$$\Delta t = \mathrm{CFL} \cdot \min\left(\frac{\Delta x}{\alpha_x}, \frac{\Delta y}{\alpha_y}\right), \tag{22}$$

where a CFL number of 0.5 is chosen for all the 2D benchmark problems reported in Section 4 below.

4. Numerical Validation and Discussion

In this section, the numerical performance, in terms of accuracy, efficiency, robustness, and stability, of the proposed finite-volume WENO-θ6 method is compared with other WENO methods. These include the fifth-order upwind WENO-Z5 [19, 20] and the sixth-order central WENO-Z6 methods [24]. These validation tests demonstrate the capability of the proposed method in both sharply capturing shock discontinuities and resolving fine vortical structures, indicating the feasibility in employment of the method for accurately modeling of complex wave interactions.

4.1. Diagonal Density Wave Advection

In this test, we verify the theoretical accuracy orders of our proposed finite-volume WENO-θ6 method, together with other compared WENO-Z5 and WENO-Z6 methods.

We set up our problem with the following initial flow configuration.

$$\begin{cases} \rho(x, y, 0) = 1 + 0.2\sin(\pi x)\sin(\pi y), \\ u(x, y, 0) = 1, v(x, y, 0) = 1, \\ p(x, y, 0) = 1. \end{cases} \tag{23}$$

Here, the exact solution, which is a diagonal advection of the density, is available. A computational domain $(\mathrm{x}, \mathrm{y}) \in [0,2]^2$ with periodic conditions applied to all boundaries. We run the simulation to the final time $\mathrm{T} = 2$ for a complete period. We select $\Delta t = \Delta x^{5/3}$ for WENO-Z5, and $\Delta t = \Delta x^2$ for WENO-Z6 and WENO-θ6 to guarantee the dominance of the spatial errors.

Table 1. *Numerical errors and accuracy orders of the WENO-Z5, WENO-Z6, and WENO-θ6 methods for the diagonal density wave advection problem (23). N is the number of grid cells per direction*

WENO-Z5						
N	**L1 error**	**order**	**L2 error**	**order**	**L∞ error**	**order**
10	1.6355e-02	—	9.7125e-03	—	9.3915e-03	—
20	5.2251e-04	**4.968**	3.2087e-04	**4.920**	3.1503e-04	**4.898**
40	1.6551e-05	**4.980**	1.0195e-05	**4.976**	1.0155e-05	**4.955**
80	5.1976e-07	**4.993**	3.2046e-07	**4.992**	3.2013e-07	**4.987**
160	1.6262e-08	**4.998**	1.0030e-08	**4.998**	1.0028e-08	**4.997**
WENO-Z6						
N	**L1 error**	**order**	**L2 error**	**order**	**L∞ error**	**order**
10	3.6621e-03	—	2.3882e-03	—	3.3542e-03	—
20	5.3536e-05	**6.096**	3.3718e-05	**6.146**	5.3658e-05	**5.966**
40	4.3716e-07	**6.936**	2.6026e-07	**7.017**	3.7979e-07	**7.142**
80	5.5677e-09	**6.295**	3.1082e-09	**6.388**	3.0129e-09	**6.978**
160	8.4766e-11	**6.037**	4.7364e-11	**6.036**	3.8265e-11	**6.299**
WENO-θ6						
N	**L1 error**	**order**	**L2 error**	**order**	**L∞ error**	**order**
10	1.2248e-03	—	6.9938e-04	—	4.7312e-04	—
20	2.1252e-05	**5.849**	1.1873e-05	**5.880**	8.3946e-06	**5.817**
40	3.4070e-07	**5.963**	1.8940e-07	**5.970**	1.3391e-07	**5.970**
80	5.3561e-09	**5.991**	2.9747e-09	**5.993**	2.1042e-09	**5.992**
160	8.4356e-11	**5.989**	4.7130e-11	**5.980**	3.6863e-11	**5.835**

The numerical errors measured in the L_1, L_2, and L_∞ norms are tabulated in Table 1, and plotted in Figure 2 (L_2 errors excluded). It is evident that all WENO schemes achieve the theoretically designed accuracy orders.

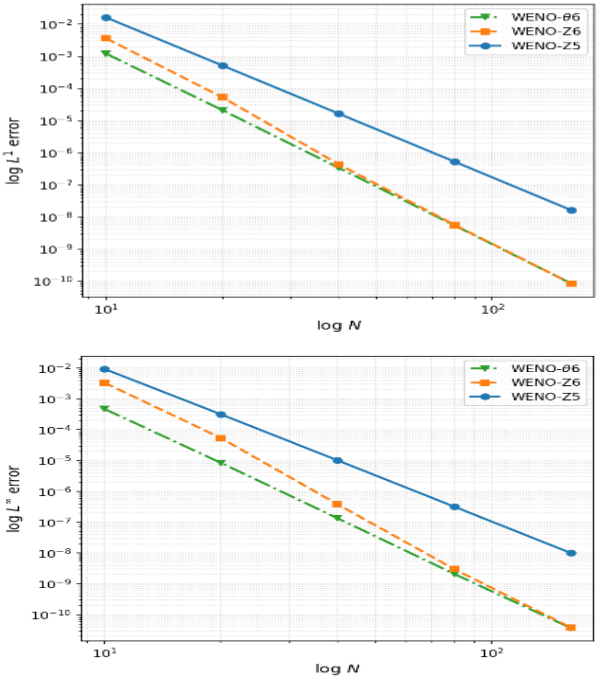

Figure 2. *Error convergence in a log-log scale of the WENO-Z5, WENO-Z6, and WENO-θ6 methods for the diagonal density wave advection problem (23). (**Top**) L_1 errors; (**Bottom**) L_∞ errors*

4.2. Shock Tube Problems

This test compares the shock-capturing capabilities of the proposed WENO-θ6 method with the WENO-Z5 and WENO-Z6 methods. For this objective, we run the 1D shock tube problems with our 2D Euler solver in the x-direction, whereas all variables are set uniformly in the y-direction. We run the test with various grid levels $N_x = 50, 100, 150, 200$ (x-direction) while fix $N_y = 10$ (y-direction). We consider the following shock tube problems:

The Sod problem:

$$(\rho, u, v, p) = \begin{cases} (0.125, 0, 0, 0.1), -5 < x < 0, \\ (1, 0, 0, 1), 0 < x < 5; \end{cases} \tag{24a}$$

and the final time T = 1.7, and

The Lax problem:

$$(\rho, u, v, p) = \begin{cases} (0.445, 0.698, 0, 3.528), -5 < x < 0, \\ (0.5, 0, 0, 0.571), 0 < x < 5; \end{cases} \tag{24b}$$

and the final time T = 1.3, and

The 123 problem:

$$(\rho, u, v, p) = \begin{cases} (1, -2, 0, 0.4), -5 < x < 0, \\ (1, 2, 0, 0.4), 0 < x < 5; \end{cases} \tag{24c}$$

and the final time T = 1. For these tests, we apply fixed conditions on the x and y-direction boundaries.

In Tables 2a and 2b, we compare the number of grid cells required to capture solution discontinuities and the approximate jump heights across these discontinuities, of all WENO methods for the Sod and the Lax problems, respectively. Here, a grid cell is counted as required to resolve a discontinuous jump providing that its density diverges from the exact left or right states of the jump by an amount of 5% of the jump height. The data shows that WENO-θ6 and WENO-Z6 capture shocks or contacts sharper than WENO-Z5 in terms of a smaller number of grid cells involved in resolving these discontinuous regions. In addition, WENO-θ6 gives the best jump height approximations among the three methods. These findings are selectively visualized for the grid case $N = 150$ in Figures 3a and 3b.

In Figure 3c, the numerical solutions for the density for the 123 problem Eq. (24c) obtained from all WENO schemes are visualized on a grid of N = 150 in the x-direction at the final time T = 1. This is an extreme test since there exists a near-vacuum junction in-between two rarefaction spanning regions. We chose p= 2 in Eq. (10), and $\alpha_R = 1$ in Eq. (16) for the WENO-θ6 method. It shows that all WENO schemes are robust for this near-vacuum benchmark problem.

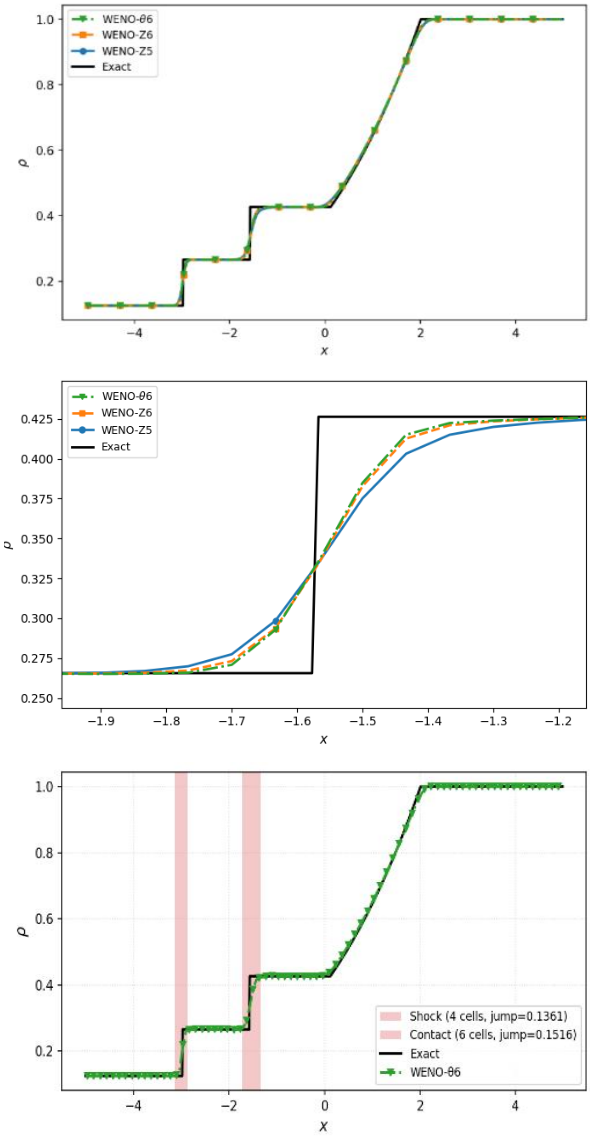

Figure 3a*. The Sod problem (24a). (**Top**) Numerical solutions for the density with a grid $N = 150$ in the x-direction for all WENO methods; (**Middle**) Zoom-in on the contact; (**Bottom**) Highlights of the grid cells to resolve discontinuous regions of the WENO-θ6 method*

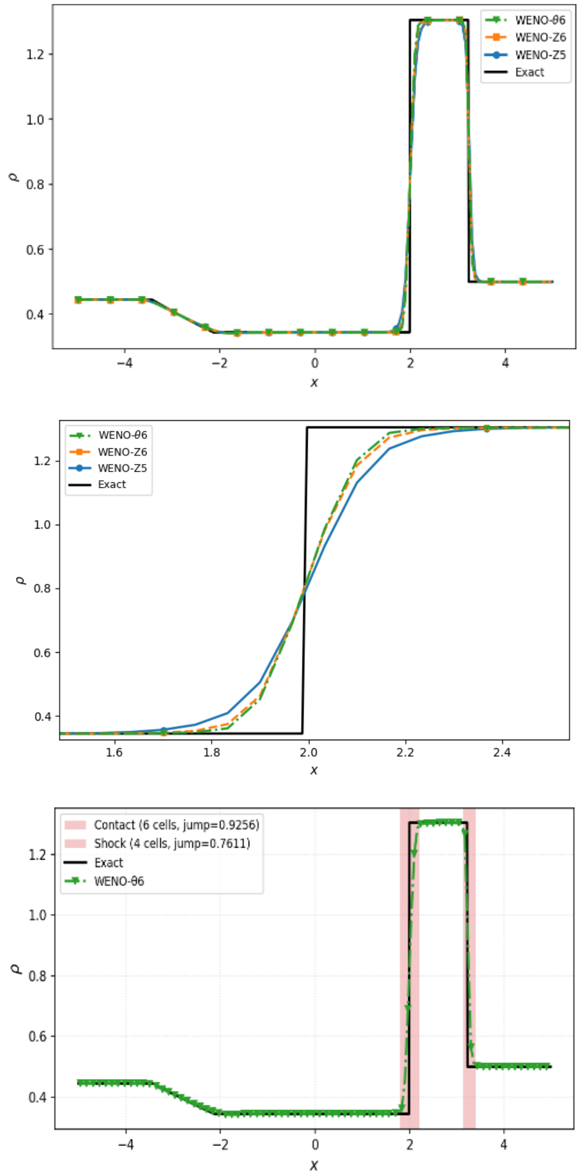

Figure 3b. *The Lax problem (24b). (Top) Numerical solutions for the density with a grid* $N = 150$ *in the x-direction for all WENO methods; (Middle) Zoom-in on the contact; (Bottom) Highlights of the grid cells to resolve discontinuous regions of the WENO-θ6 method*

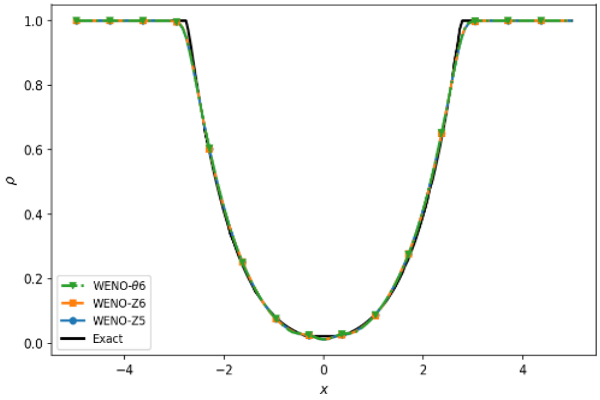

Figure 3c. *The 123 problem (24c). Numerical solutions for the density with a grid* $N = 150$ *in the x-direction for all WENO methods*

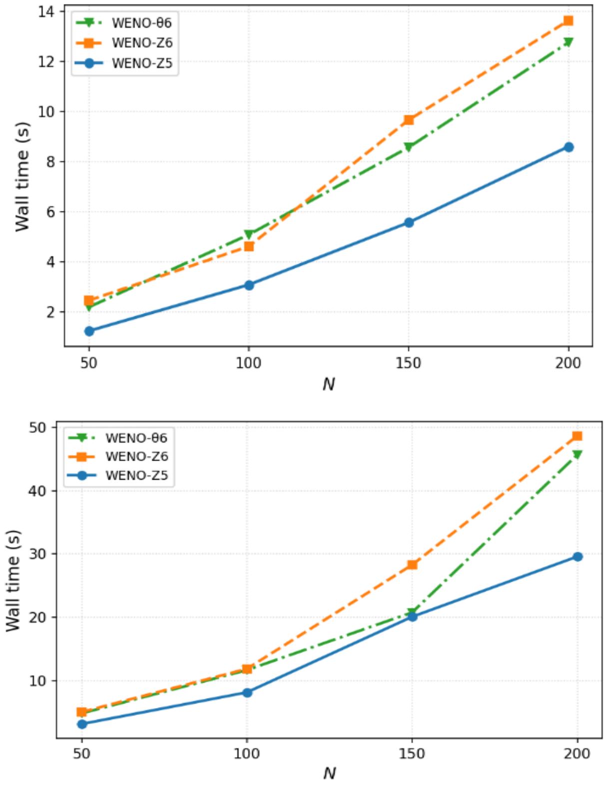

Figure 4. *Measured wall time (seconds) for all WENO methods at different grid levels. N is the number of grid cells in the x-direction. (**Top**) The Sod problem (24a); (**Bottom**) The Lax problem (24b)*

Table 2a. *The Sod problem (24a): Number of grid cells required to resolve shocks or contacts at different grid levels, together with the captured jump heights (values in parentheses). The exact jump height at the shock is 0.1406; at the contact is 0.1607*

Discontinuity	N = 50	N = 100	N = 150	N = 200
WENO-θ6				
Shock: x = -2.9785	4 (0.1363)	4 (0.1370)	4 (0.1361)	4 (0.1368)
Contact: x = -1.5723	5 (0.1480)	6 (0.1523)	6 (0.1516)	6 (0.1527)
WENO-Z6				
Shock: x = -2.9785	4 (0.1369)	4 (0.1374)	4 (0.1376)	4 (0.1381)
Contact: x = -1.5723	6 (0.1490)	6 (0.1484)	6 (0.1479)	6 (0.1475)
WENO-Z5				
Shock: x = -2.9785	4 (0.1289)	4 (0.1294)	5 (0.1352)	5 (0.1357)
Contact: x = -1.5723	8 (0.1526)	8 (0.1510)	8 (0.1501)	8 (0.1494)

Table 2b. *The Lax problem (24b): Number of grid cells required to resolve shocks or contacts at different grid levels, together with the captured jump heights (values in parentheses). The exact jump height at the contact is 0.9595; at the shock is 0.8041*

Discontinuity	N = 50	N = 100	N = 150	N = 200
WENO-θ6				
Contact: x = 1.9922	6 (0.9516)	6 (0.9344)	6 (0.9256)	6 (0.9186)
Shock: x = 3.2227	4 (0.7731)	5 (0.7935)	4 (0.7611)	4 (0.7644)
WENO-Z6				
Contact: x = 1.9922	6 (0.9264)	6 (0.9096)	6 (0.8975)	6 (0.8879)
Shock: x = 3.2227	4 (0.7629)	5 (0.7925)	4 (0.7603)	4 (0.7732)
WENO-Z5				
Contact: x = 1.9922	6 (0.8745)	8 (0.9145)	8 (0.9039)	8 (0.8963)
Shock: x = 3.2227	5 (0.7642)	5 (0.7645)	5 (0.7638)	5 (0.7618)

We turn our attention to compare the computational times for all WENO schemes at different grid levels. In Figure 4, the running wall times of all schemes are plotted against the grid levels for both the Sod and the Lax problems. The visualized data demonstrates the outperformance of WENO-θ6 comparing with the other WENO methods. Firstly, WENO-θ6 resolves the discontinuities much sharper than WENO-Z5 to trade-off its higher computational cost. Secondly, WENO-θ6 is cheaper than WENO-Z6 yet is capable to resolve shocks and contacts more satisfactorily.

4.3. Rayleigh – Taylor Instability

We choose to simulate the Rayleigh – Taylor instability test [31]. The instability occurs when there is a heavier fluid falling into a lighter fluid. The problem setup is configurated as follows. We select the domain $(x, y) \in [-0.25, 0.25] \times [-0.75, 0.75]$. The initial condition is specified below.

$$\begin{cases} \rho = 2\ (y \geq 0), \rho = 1\ (y < 0), \\ u = 0, \\ v = \frac{0.01}{4}(1 + \cos(4\pi x))\left(1 + \cos\left(\frac{4}{3}\pi y\right)\right), \\ p = 2.5 - \rho g y. \end{cases} \tag{25}$$

Here, $g = 0.1$ is the gravitational acceleration. Body forcing terms $-g\rho$ and $-g\rho v$ are added in the y-momentum and energy equations, respectively, in the Euler governing equations. Periodic boundary conditions are supplemented in the x-direction, and reflective conditions are set for the boundaries on the y-direction.

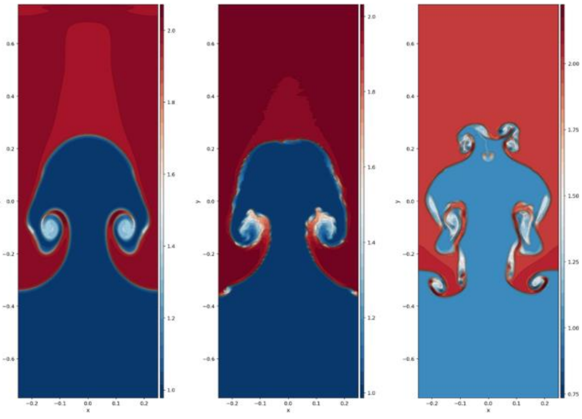

Figure 5. *The Rayleigh – Taylor instability Eq. (25). Numerical solutions for the density with a grid* 240×720. *Contour plot with 30 equally spaced contours at the final time* $T = 9.5$. ***(Left)*** *WENO-Z5;* ***(Middle)*** *WENO-Z6;* ***(Right)*** *WENO-θ6*

The density contours at the final time obtained from all WENO methods are visualized in Figure 5 on a grid 240×720. The figure clearly show that WENO-θ6 is able to resolve secondary small-scaled structures, e.g., KH vortices, much better than the compared WENO-Z5 and WENO-Z6 methods. This, in turn, infers that WENO-θ6 is the least dissipative method among the three for this benchmark.

4.4. 2D Implosion

For the 2D implosion problem, a quadrant of a square computational domain containing a fluid with lower density and pressure is compressed by a surrounding denser fluid with higher pressure initially. As a result, the quadrant experiences a self-implosion to create jets along the diagonal. Symmetry is crucial for this benchmark. In addition, a method with higher numerical dispersion results in longer and narrower diagonal jets [32]. The initial condition of the 2D implosion is specified as follows.

$$(\rho, u, v, p) = \begin{cases} (1, 0, 0, 1)\ for\ x + y > \frac{1}{2}, \\ (0.125, 0, 0, 0.14)\ otherwise; \end{cases} \tag{26}$$

with reflective boundary conditions applied to all walls. The simulation is run to the final time $T = 5$.

In Figure 6, thirty equally spaced density contours are plotted on a grid 250×250 for all WENO schemes. For this test, we choose $\alpha_R = 1$ for the WENO-θ6 method. Our proposed method again outperforms the other two with visible narrow jet projected along the main diagonal of the domain. We also note that problem symmetry is well preserved for this test, especially for WENO-θ6.

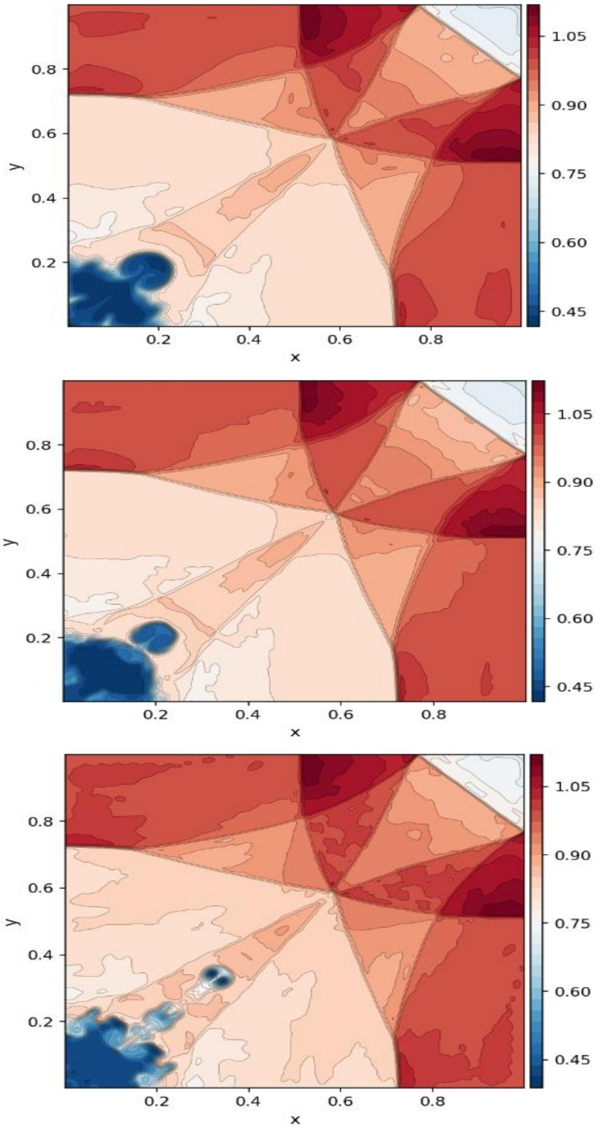

Figure 6. *The 2D implosion Eq. (26). Numerical solutions for the density with a grid* 250×250. *Contour plot with 30 equally spaced contours at the final time* $T = 5$. ***(Top)*** *WENO-Z5;* ***(Middle)*** *WENO-Z6;* ***(Bottom)*** *WENO-θ6*

4.5. Double Mach Reflection of a Strong Shock

The Double Mach Reflection (DMR) problem [33] tests the capability of high-order schemes in approximate the solution under an extreme problem setting: a Mach-10 shock strikes a wedge at 30^0. The domain starts at $\Omega = [0,4] \times [0,1]$, with the shock which is initialized by the Rankine-Hugoniot conditions:

$$(\rho, u, v, p) = \begin{cases} (8, 8.25\cos 30°, -8.25\sin 30°, 116.5), & x < x_0 + \frac{y}{\tan 60°}, \\ (1.4, 0, 0, 1), & x \geq x_0 + \frac{y}{\tan 60°}. \end{cases} \quad (27)$$

The simulation advances to the final time T = 2. A reflective condition is imposed on the bottom boundary, with the shock prescribed at the top to maintain consistency.

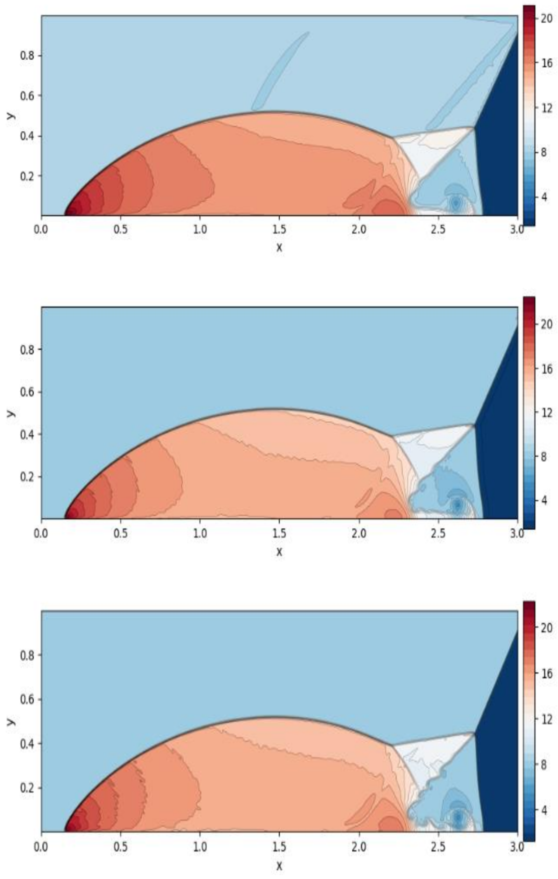

Figure 7. *The Double Mach reflection Eq. (27). Numerical solutions for the density at a grid 800×200. Contour plot with 30 equally spaced contours at the final time* $T = 2$.
(Top) *WENO-Z5;* ***(Middle)*** *WENO-Z6;* ***(Bottom)*** *WENO-θ6*

In Figure 7, we plot the density contours obtained by the three WENO methods on a grid of 800×200. The results clearly reveal that our proposed method is able to capture the bow shock, the Mach stem, and the triple point sharply without spurring non-physical oscillations near these discontinuous areas, which in turn secures the numerical stability, even for this highly extreme problem. In addition, secondary KH vortices and structures are captured and resolved with increasing detail as the grid is refined, with wavelengths decreasing towards the inviscid limit. Among the comparing methods, WENO-θ6 exhibits the best resolution in terms of clearly visualized details of secondary KH vortical structures.

4.6. Mach 3 Wind Tunnel with a Forward-Facing Step

The Mach 3 forward-facing step problem is designed to test whether a high-order method can resolve shock-wall interactions and shear layer formulation on a sharp corner. The testing computational domain on a [0,3] x [0,1] area in which a horizontal step of 0.2-unit height is present at *x = 0.6*. Initially, a Mach-3 fluid flow is configurated as follows.

$$(\rho, u, v, p) = (1.4, 3, 0, 1) \quad (28)$$

A reflective wall condition is applied on the top and bottom boundaries, whereas an inflow and outflow condition are deployed for the left and right boundaries, respectively. We run the simulation to the final time T = 4 to reach a steady-state solution.

As pointed out by Balsara et al. [16], simulations with sharp corners in the domain pose enormous challenges to many upwind schemes without an artificial entropy-fix mechanism.

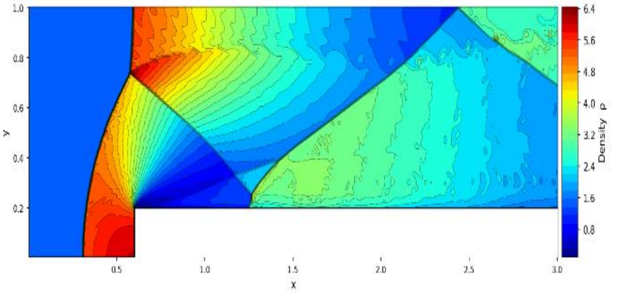

Figure 8. *The Mach 3 wind tunnel with a forward-facing step Eq. (28). Numerical solutions obtained by the WENO-θ6 method for the density at a grid 600×200. Contour plot with 30 equally spaced contours at the final time* $T = 4$

The result of density contours obtained by the WENO-θ6 is presented in Figure 8. It is evident that the contact discontinuity from the post-shock to expansion region remains sharp without smearing, which in turn illustrates the capability of the scheme to handle shocks effectively.

4.7. The 2D Riemann Problem

The 2D Riemann problem tests numerical schemes across all wave types and interactions, including rarefaction (4R), four-shock (4S), four-contact (4J), mixed contact-rarefaction (2J+2R), mixed contact-shock (2J+2S), and full-spectrum mixed-wave (2J+R+S). There are 19 unique configurations. Simulations use a uniform grid with outflow boundary conditions and CFL 0.5. Density contours of selectively chosen configurations are plotted at the final time on a fine grid 1200×1200. The initial conditions and wave structures are in the supplementary materials [34]. For each configuration, we run the simulation until the final T, and the density contours are plotted in Figure 9. For all these different settings of the 2D Riemann problem, our proposed scheme is proven to excel at both tackling shock regions without creating oscillations, while resolving high-detailed small-scale structures in smooth areas. We notice that vortical structures like KH instabilities have grid-converged wavelengths; this confirms the WENO-θ6 scheme to possess good physical resolution, low numerical dissipation, and solution symmetry sustainability.

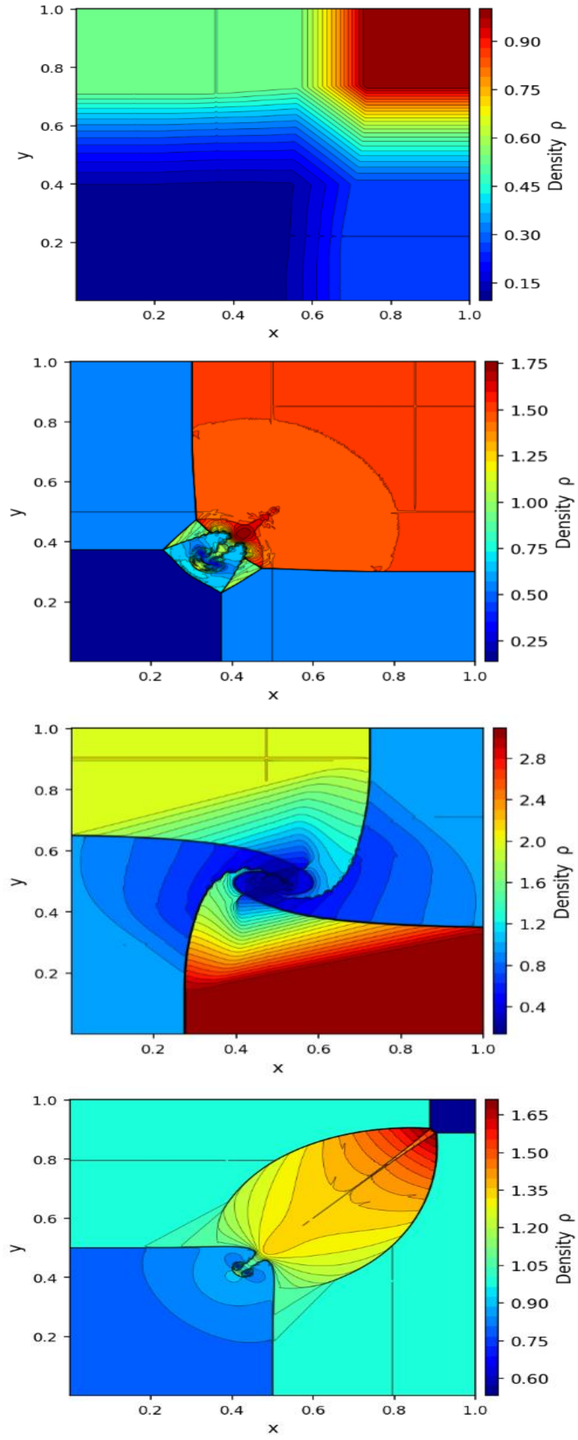

***Figure 9.** The 2D Riemann problem. Numerical solutions obtained by the WENO-θ6 method for the density at a fine grid 1200× 1200. Contour plot with 30 equally spaced contours at the final time. (**From top down**) Configuration 1; Configuration 3; Configuration 6; and Configuration 12*

Configuration 1: $\overleftarrow{R}_{21}\,\overleftarrow{R}_{32}\,\overleftarrow{R}_{34}\,\overleftarrow{R}_{41}$ $(T = 0.15)$. Four backward rarefaction waves expand from the center, creating a near-vacuum, low-density, low-pressure core, highlighting the scheme's positivity preservation in extreme rarefaction.

Configuration 3: $\overleftarrow{S}_{21}\,\overleftarrow{S}_{32}\,\overleftarrow{S}_{34}\,\overleftarrow{S}_{41}$ $(T = 0.30)$. Four converging shocks generate a dense, high-pressure central jet with strong shear. The solution clearly shows Kelvin-Helmholtz roll-ups along slip lines, testing the scheme's low numerical dissipation and fine-structure resolution.

Configuration 6: $J_{21}^{-}\,J_{32}^{+}\,J_{34}^{-}\,J_{41}^{+}$ $(T = 0.30)$. Alternating contact orientations generate a spiral vortex pattern with secondary instabilities along the arms, serving as a key isotropy test for dimension-split schemes.

Configuration 12: $\overrightarrow{S_{21}}\,J_{32}^{+}\,J_{34}^{+}\,\overrightarrow{S_{41}}$ $(T = 0.25)$. In this strongly asymmetric wave configuration, the interaction of two forward shocks with two contact discontinuities produces a diagonally elongated high-density lobe and a central spiral vortex. The approximate solution exhibits sharp shocks, clear slip lines, and a steep density contrast with minimal spurious oscillations.

5. Conclusion

This paper presents and tests a high-order FV WENO-θ6 scheme for the 2D compressible Euler equations, using an adaptive weight optimization strategy in a DbD FVM framework. The scheme reduces numerical dissipation while keeping shock-capturing stability, reaches sixth-order accuracy in smooth areas, and switches to a stable, non-oscillatory mode near discontinuities using smoothness-based adaptive weighting, without artificial viscosity or entropy fixes. The proposed WENO-θ6 outperforms other compared methods in various tough benchmark problems, which in turns numerically validates the scheme capabilities in resolving fine vortical structures, capturing sharp shocks, and complex wave interactions in a strictly conservative framework. The DbD reconstruction is as efficient as standard methods but offers high resolution similar to more expensive multidimensional schemes. In the future, we plan to extend this approach to unstructured meshes as well as add diffusion terms for the Navier-Stokes equations, making the scheme more adaptable for real engineering problems.

Acknowledgements: This work was funded by the Vietnamese Ministry of Education and Training (grant B2024-VGU-06).

REFERENCES

[1] E. F. Toro, *Riemann solvers and numerical methods for fluid dynamics: a practical introduction*, 3rd ed. Dordrecht New York: Springer, 2009.

[2] D. Christodoulou, "The Euler Equations of Compressible Fluid Flow," *Bull. Am. Math. Soc.,* vol. 44, no. 4, pp. 581–602, 2007.

[3] O. Darrigol and U. Frisch, "From Newton's mechanics to Euler's equations," *Phys. Nonlinear Phenom.*, vol. 237, no. 14–17, pp. 1855–1869, 2008.

[4] H. Alfvén, "Existence of Electromagnetic-Hydrodynamic Waves," *Nature,* vol. 150, no. 3805, pp. 405–406, 1942.

[5] D. P. Hampshire, "A derivation of Maxwell's equations using the Heaviside notation," *Philos. Trans. R. Soc. Math. Phys. Eng. Sci.*, vol. 376, no. 2134, p. 20170447, 2018.

[6] J. D. Jackson, *Classical electrodynamics,* 3. ed., [Nachdr.]. Hoboken, NY: Wiley, 2009.

[7] A. Harten, "High resolution schemes for hyperbolic conservation laws," *J. Comput. Phys.*, vol. 49, no. 3, pp. 357–393, 1983.

[8] A. Harten, “On a Class of High Resolution Total-Variation-Stable Finite-Difference Schemes,” *SIAM J. Numer. Anal., v*ol. 21, no. 1, pp. 1–23, 1984.

[9] A. Harten and S. Osher, “Uniformly High-Order Accurate Nonoscillatory Schemes. I,” S*IAM J. Numer. Anal.,* vol. 24, no. 2, pp. 279–309, 1987.

[10] A. Harten, B. Engquist, S. Osher, and S. R. Chakravarthy, “Uniformly High Order Accurate Essentially Non-oscillatory Schemes, III,” *J. Comput. Phys.*, vol. 131, no. 1, pp. 3–47, 1997.

[11] C.-W. Shu and S. Osher, “Efficient implementation of essentially non-oscillatory shock-capturing schemes,” *J. Comput. Phys.,* vol. 77, no. 2, pp. 439–471, 1988.

[12] C.-W. Shu and S. Osher, “Efficient implementation of essentially non-oscillatory shock-capturing schemes, II,” *J. Comput. Phys*., vol. 83, no. 1, pp. 32–78, 1989.

[13] X.-D. Liu, S. Osher, and T. Chan, “Weighted Essentially Non-oscillatory Schemes,” *J. Comput. Phys.,* vol. 115, no. 1, pp. 200–212, 1994.

[14] G.-S. Jiang and C.-W. Shu, “Efficient Implementation of Weighted ENO Schemes,” *J. Comput. Phys.,* vol. 126, no. 1, pp. 202–228, 1996.

[15] C.-W. Shu, “High-order Finite Difference and Finite Volume WENO Schemes and Discontinuous Galerkin Methods for CFD,” *Int. J. Comput. Fluid Dyn.,* vol. 17, no. 2, pp. 107–118, 2003.

[16] D. S. Balsara and C.-W. Shu, “Monotonicity Preserving Weighted Essentially Non-oscillatory Schemes with Increasingly High Order of Accuracy,” *J. Comput. Phys.*, vol. 160, no. 2, pp. 405–452, 2000.

[17] X. Ji and Y. Zheng, “Characteristic decouplings and interactions of rarefaction waves of 2D Euler equations,” *J. Math. Anal. Appl.*, vol. 406, no. 1, pp. 4–14, 2013.

[18] A. K. Henrick, T. D. Aslam, and J. M. Powers, “Mapped weighted essentially non-oscillatory schemes: Achieving optimal order near critical points,” *J. Comput. Phys.,* vol. 207, no. 2, pp. 542–567, 2005.

[19] R. Borges, M. Carmona, B. Costa, and W. S. Don, “An improved weighted essentially non-oscillatory scheme for hyperbolic conservation laws,” *J. Comput. Phys.*, vol. 227, no. 6, pp. 3191–3211, 2008.

[20] M. Castro, B. Costa, and W. S. Don, “High order weighted essentially non-oscillatory WENO-Z schemes for hyperbolic conservation laws,” *J. Comput. Phys.,* vol. 230, no. 5, pp. 1766–1792, 2011.

[21] N. K. Yamaleev and M. H. Carpenter, “A systematic methodology for constructing high-order energy stable WENO schemes,” J. Comput. Phys., vol. 228, no. 11, pp. 4248–4272, 2009.

[22] M. H. Carpenter, T. C. Fisher, and N. K. Yamaleev, “Boundary Closures for Sixth-Order Energy-Stable Weighted Essentially Non-Oscillatory Finite-Difference Schemes,” in Advances in Applied Mathematics, Modeling, and Computational Science, vol. 66, R. Melnik and I. S. Kotsireas, Eds., in Fields Institute Communications, vol. 66, Boston, MA: Springer US, 2013. DOI: https://doi.org/10.1007/978-1-4614-5389-5_6

[23] X. Y. Hu, Q. Wang, and N. A. Adams, “An adaptive central-upwind weighted essentially non-oscillatory scheme,” *J. Comput. Phys*., vol. 229, no. 23, pp. 8952–8965, 2010.

[24] F. Hu, “The 6th-order weighted ENO schemes for hyperbolic conservation laws,” *Comput. Fluids,* vol. 174, pp. 34–45, 2018.

[25] C. Huang and L. L. Chen, “A new adaptively central-upwind sixth-order WENO scheme,” *J. Comput. Phys*., vol. 357, pp. 1–15, 2018.

[26] K. Zhao, Y. Du, and L. Yuan, “A New Sixth-Order WENO Scheme for Solving Hyperbolic Conservation Laws,” *Commun. Appl. Math. Comput.*, vol. 5, no. 1, pp. 3–30, 2023.

[27] C.-Y. Jung and T. B. Nguyen, “A new adaptive weighted essentially non-oscillatory WENO- θ scheme for hyperbolic conservation laws,” *J. Comput. Appl. Math*., vol. 328, pp. 314–339, 2018.

[28] N. M. H. Pham and T. B. Nguyen, “High-Order Finite-Volume Weighted Essentially Non-Oscillatory WENO-THETA6 Method for the Unsteady Euler Equations in One-Dimensional Computational Fluid Dynamics Simulations”. *UD-JST*, vol. 23, no. 6A, pp. 74–80, 2025.

[29] E. M. Taylor, M. Wu, and M. P. Martín, “Optimization of nonlinear error for weighted essentially non-oscillatory methods in direct numerical simulations of compressible turbulence,” *J. Comput. Phys.*, vol. 223, no. 1, pp. 384–397, 2007.

[30] S. Gottlieb and C.-W. Shu, “Total variation diminishing Runge-Kutta schemes,” *Math. Comput.*, vol. 67, no. 221, pp. 73–85, 1998.

[31] C. L. Gardner, J. Glimm, O. McBryan, R. Menikoff, D. H. Sharp, and Q. Zhang, “The dynamics of bubble growth for Rayleigh–Taylor unstable interfaces,” *Phys. Fluids,* vol. 31, no. 3, pp. 447–465, 1988.

[32] R. Liska and B. Wendroff, “Comparison of Several Difference Schemes on 1D and 2D Test Problems for the Euler Equations,” *SIAM J. Sci. Comput.,* vol. 25, no. 3, pp. 995–1017, 2003.

[33] P. Woodward and P. Colella, “The numerical simulation of two-dimensional fluid flow with strong shocks,” J. *Comput. Phys.,* vol. 54, no. 1, pp. 115–173, 1984.

[34] C.-Y. Jung and T. B. Nguyen, “Fine structures for the solutions of the two-dimensional Riemann problems by high-order WENO schemes,” *Adv. Comput. Math.,* vol. 44, no. 1, pp. 147–174, 2018.